Supplementary Information

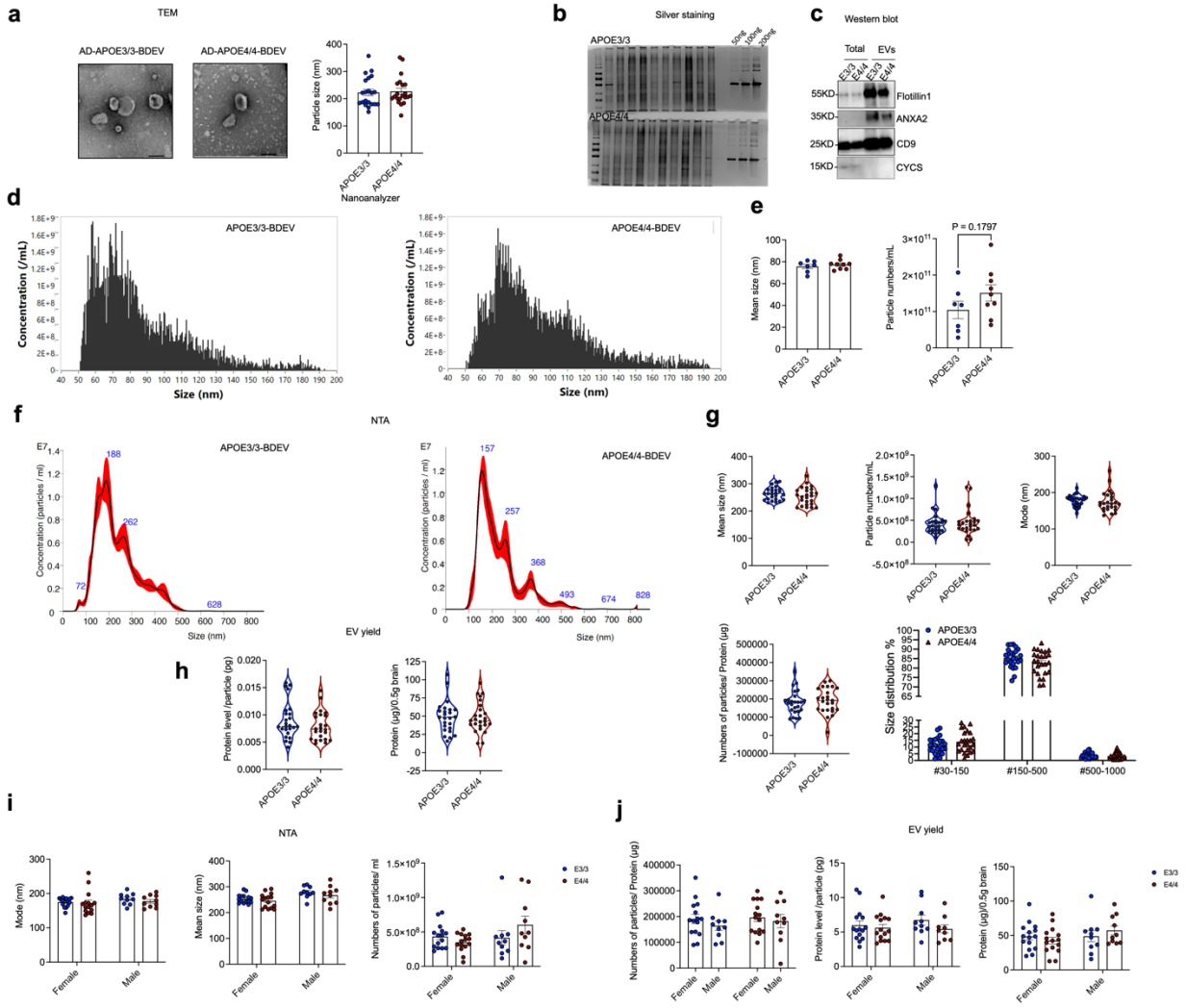

Extended Fig. 1: Characterization of APOE3/3 and APOE4/4 AD-BDEVs and the influence of sex on their properties.

a, Transmission electron microscopy (TEM) images showing the round cup-shaped and intact morphology of BDEVs isolated from APOE3/3 and APOE4/4 AD human brain (scale bar: 200 nm). The quantification of size distribution (diameter nm) of BDEVs from APOE3/3 (blue) and APOE4/4 (red) human AD brains. **b**, Representative silver-stained SDS-PAGE gel showed total protein profiles of BDEVs isolated from APOE3/3 and APOE4/4 AD patients. **c**, Western blot analysis of BDEV markers showed the presence of EV-specific proteins (Flotillin1, ANXA2, CD9) and non-EV protein makers (CYCS), confirming the purity of the BDEV preparations. **d**, Histograms representing the size distribution of BDEVs from APOE3/3 and APOE4/4 as measured by Flow Nanoanalyzer (NanoFCM). **e**, Dot plots showed mean particle size and concentration, indicating no significant differences between the genotypes. **f**, Nanoparticle tracking analysis (NTA) displayed the size distribution and concentration of particles in APOE3/3 and APOE4/4 BDEV samples. **g**, Violin plot graphs showed mean size, particle

concentration, mode size, number of particles per microgram of protein and size distribution for BDEVs from APOE3/3 and APOE4/4 BDEVs. No significant differences were observed across all parameters. **h**, Quantification of protein yield including protein level per particle, protein level per 0.5 gram of brain tissue as violin plots from APOE3/3 and APOE4/4 BDEVs showed no significant differences between genotypes. **i**, Bar graphs showed mode, mean size, and particle concentration of BDEVs from male and female APOE3/3 and APOE4/4 AD patients. **j**, Bar graphs illustrated the EV yield based on NTA data, including the number of particles per microgram of protein, protein level per particle, and protein level per 0.5 gram of brain tissue in male and female APOE3/3 and APOE4/4 AD patients. No significant sex-specific differences were observed in the data. N = 20 individual cases for each genotype, all Data are presented as mean ± SEM.

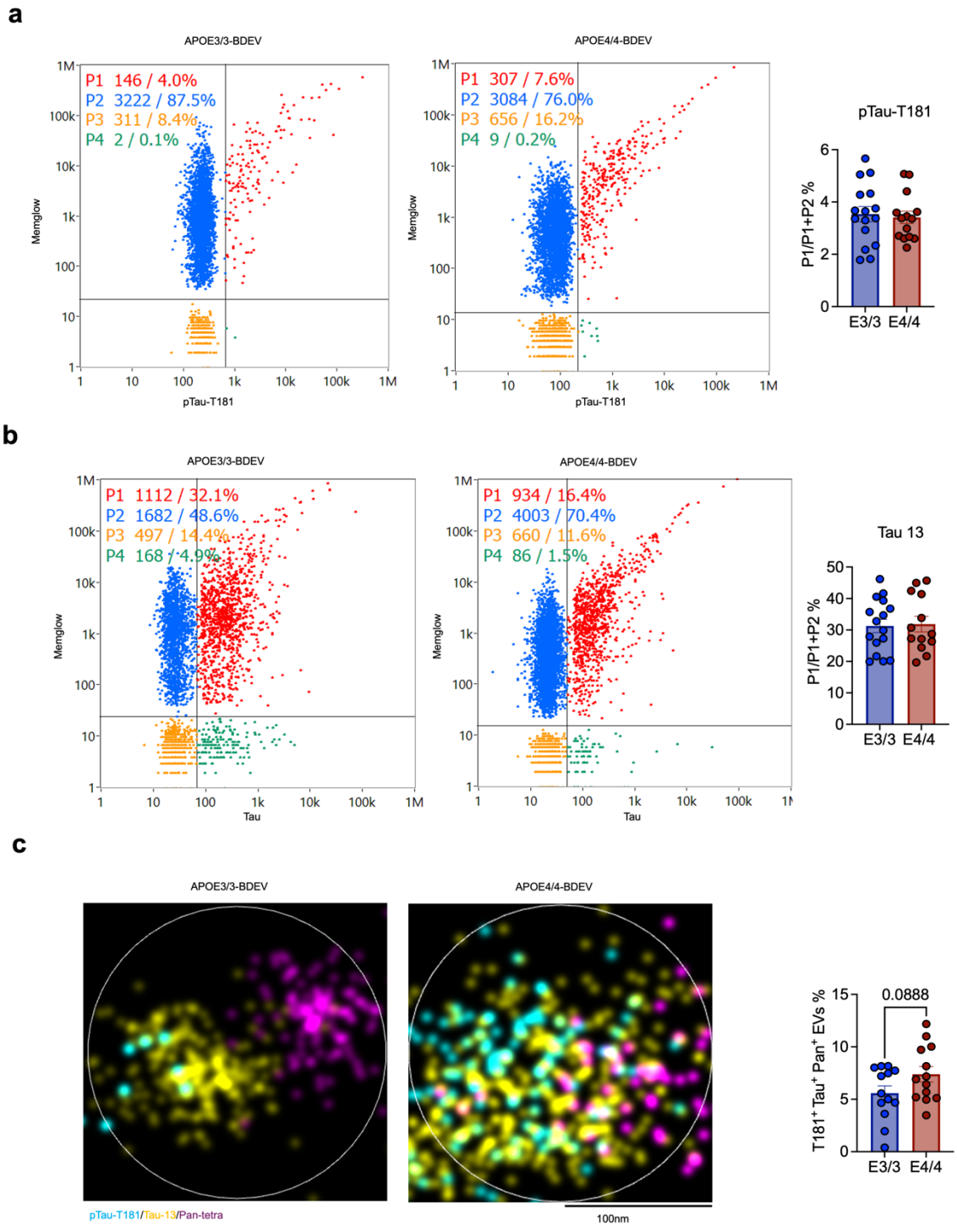

Extended Fig. 2: Nano Flow cytometry analysis for pathological markers in APOE3 and APOE4 BDEVs.

a-b, Flow Nanoanalyzer scatter plots showed pTau-T181 (**a**) and Tau13 (**b**) conjugated with Alexa Fluor 647 (x-axis) versus MemGlow 488-labeled particles (y-axis) in AD BDEVs from

APOE3/3 and APOE4/4, with overlap indicated as P1. No significant difference was observed in the P1 population between pTau-T181(**a**) and Tau13 (**b**). **c**, Super-resolution microscopy images of BDEVs showed co-localization of pTau-T181-Alex647/Tau-13-Alex594 with pan-tetraspanins CD9, CD81, and CD63 (scale bar: 100 nm). The quantification of percentage of triple $pT181^{+}$ /Tau^{+}/pan-$tetraspanins^{+}$ clusters between APOE3/3 and APOE4/4 BDEVs, indicating an increased trend in phosphorylated tau (T181) in the APOE4/4 group. All Data are presented as mean ± SEM.

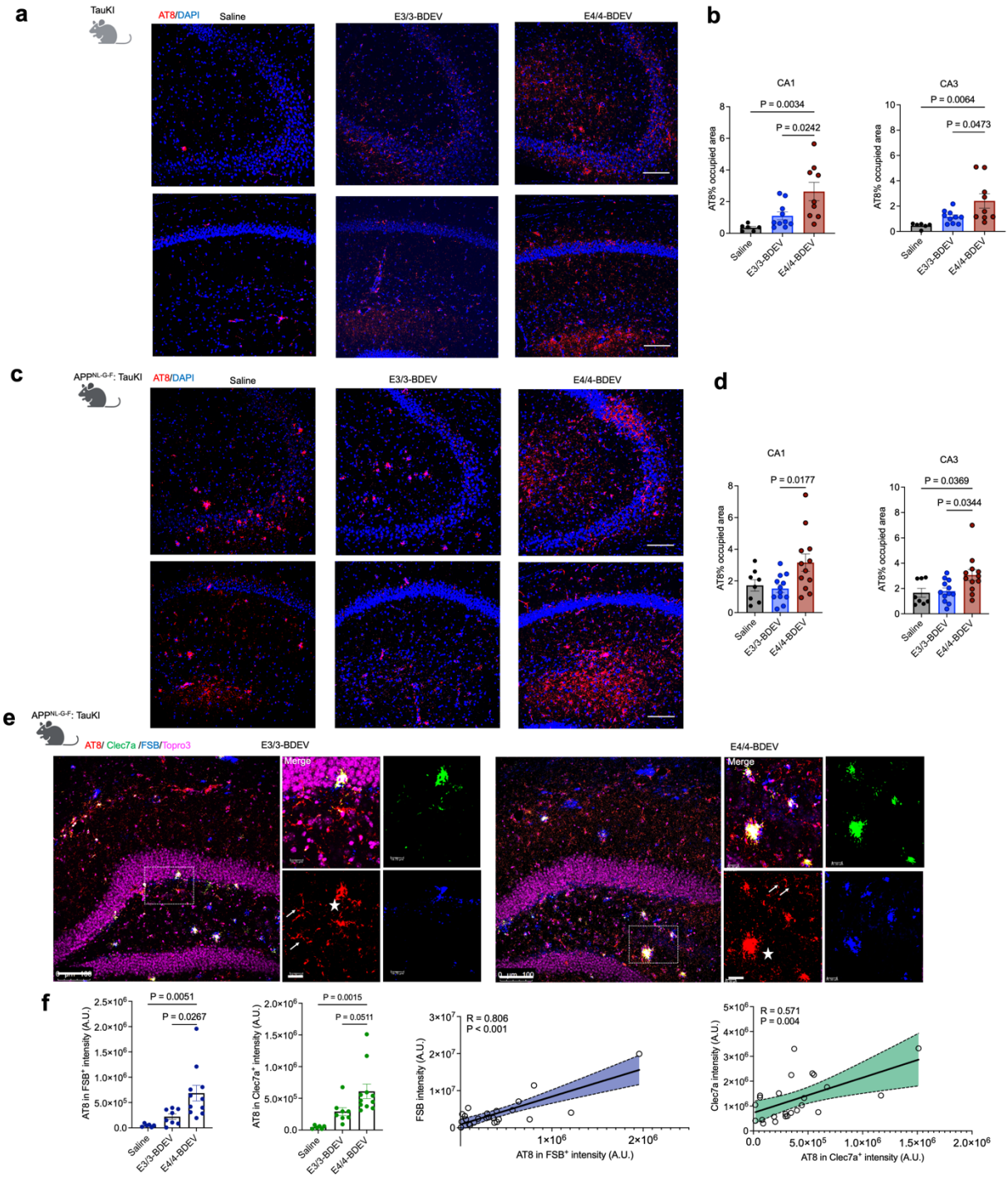

Extended Fig. 3: Tau pathology analysis with incubation of BDEV from APOE3/3 and APOE4/4 in Tau KI mice and APP/Tau KI.

a, c, Immunofluorescence staining for AT8 (red) in the CA3 and CA1 regions of the hippocampus in Tau KI mice (**a**) and APP/Tau KI mice (**c**) after intrahippocampal injection with saline, APOE3/3-BDEVs, or APOE4/4-BDEVs at 10-13 months of age. Nuclei are counterstained with DAPI (blue). Scale bar: 100 µm. **b, d,** Quantification of AT8-positive

fluorescence intensity in the CA1 and CA3 regions of Tau KI (**b**) and APP/Tau KI (**d**) mice. **e**, Representative images showed co-localization of AT8 (red) with Clec7a (green), FSB (blue), and Topro3 (magenta) in the DG of APP/Tau KI mice injected with E3/3-BDEVs or E4/4-BDEVs. White arrows indicate AT8 without co-localization with FSB and Clec7a; asterisks indicate co-localization with FSB and Clec7a. **f**, Quantification of AT8 intensity in FSB+ areas and Clec7a+ areas, respectively. Correlation analysis was performed between AT8 intensity in FSB^+ area and FSB intensity, as well as AT8 intensity in $Clec7a^+$ area and Clec7a intensity. Pearson's correlation coefficient (r) and p-value are indicated. Significant differences were determined by one-way ANOVA followed by Tukey's *post hoc* test.

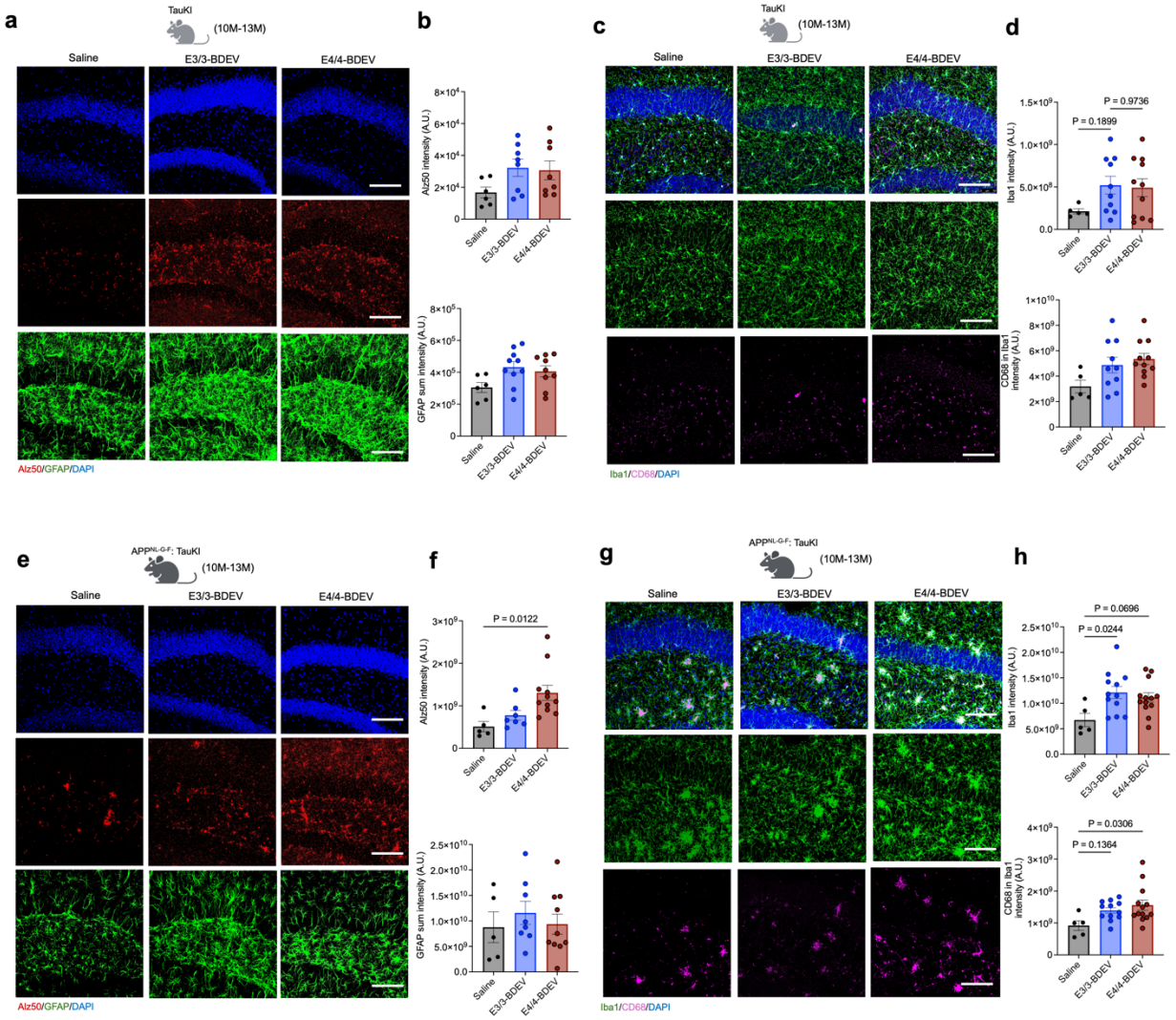

Extended Fig. 4: Neuroinflammatory and neuropathological analysis incubated with BDEV from APOE3/3 and APOE4/4 in Tau KI mice and APP/Tau KI.

a, Representative immunofluorescence images showed DAPI (blue), Alz50 (red), and GFAP (green) staining in hippocampal sections of Tau KI mice treated with saline, APOE3/3-BDEV, or APOE4/4-BDEV. **b**, Quantification of Alz50 and GFAP intensity in Tau KI mice, showed an increased trend in both APOE3/3 and APOE4/4 BDEV treatments compared with saline group. **c**, Immunofluorescence images showed Iba1 (green) and CD68 (magenta) staining in Tau KI hippocampal DG sections. **d**, Quantification of Iba1 intensity and CD68 intensity within Iba1+ microglial in Tau KI hippocampal DG. **e**, Representative immunofluorescence images showed DAPI (blue), Alz50 (red), and GFAP (green) staining in hippocampal DG sections of APP/Tau KI mice treated with saline, APOE3/3-BDEV, or APOE4/4-BDEV. **f**, Quantification of Alz50 and GFAP intensity in APP/Tau KI mice demonstrated a significant increase in Alz50 in APOE4/4-BDEV treated mice compared with the saline treated group, while GFAP staining remained unchanged. **g**, Immunofluorescence images showed Iba1 (green) and CD68 (magenta)

staining in hippocampal DG sections of APP/Tau KI. **h**, Quantification of Iba1 and CD68 intensity within Iba1+ microglia in the hippocampal DG of APP/Tau KI mice. The analysis demonstrated increased phagocytic microglial activation in APOE4/4-BDEV-treated APP/Tau KI mice compared to the saline group, whereas APOE3/3-BDEV did not show this effect. All Data are presented as mean ± SEM. One-way ANOVA followed by Tukey's *post hoc* test. Scale bar: 100 μm.

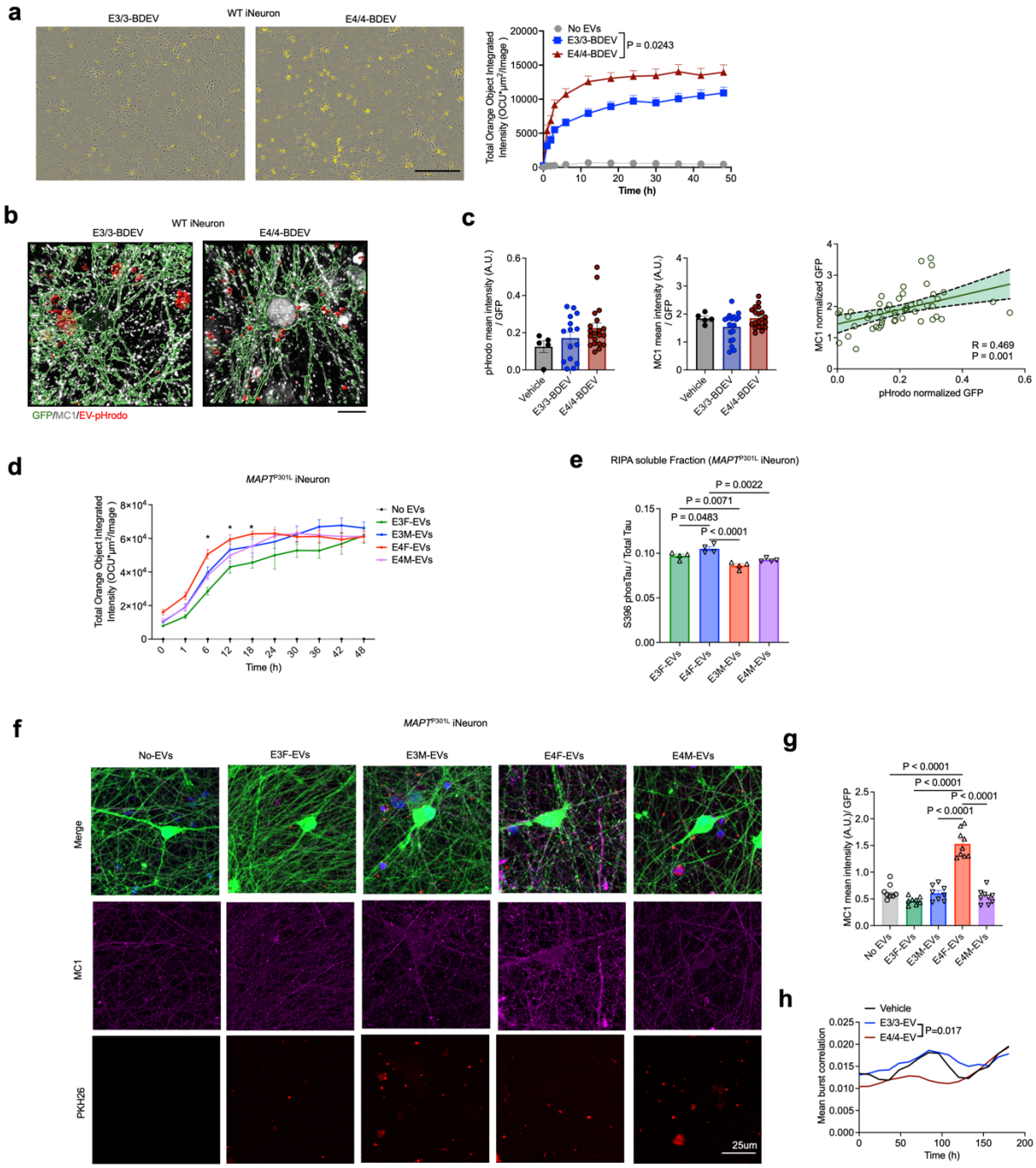

Extended Fig. 5: The effect of APOE3/3 and APOE4/4 EVs on neuronal uptake and activity and sex difference.

a, Representative images showed the uptake of APOE3/3-BDEVs and APOE E4/4-BDEVs (orange) by WT iNeurons. Scale bar: 200 µm. Quantification of the total orange object integrated intensity (OCU/µm²/image) over time indicated EV neuronal uptake in WT treated with APOE3/3-BDEVs (bule), APOE4/4-BDEVs (red) or only dye (grey). Significant differences were determined by ROC area under the curve analysis. BDEVs from three donors per group with

technical replicates. **b,** Representative 3D Imaris reconstructions showed GFP (green), misfolded tau MC1 (grey), and EV-pHrodo (red) in WT iNeurons treated with BDEVs (APOE3/3 and APOE4/4) or no EVs (vehicle). Scale bar: 5 μm. **c**, Quantification of pHrodo mean intensity and MC1 mean intensity normalized by GFP in WT iNeurons treated with different genotype EVs or vehicle (PBS) controls. Correlation analysis between pHrodo mean intensity and MC1 mean intensity in WT iNeurons. **d**, Neuronal uptake of BDEVs displayed time-dependent orange signal changes in EV uptake in *MAPT*^{P301L} iNeurons treated with BDEVs from APOE3/3 female (E3F), APOE3/3 male (E3M), APOE4/4 female (E4F), and APOE4/4 male (E4M) and dye only as controls. E4F BDEVs showed significantly increased neuronal EV uptake compared to other groups. The differences were determined as a Two-Way Repeated Measures ANOVA test. **e,** Bar graphs showed the levels of S396 phosphorylated tau normalized to total tau, in *MAPT*^{P301L} iNeurons after treatment with BDEVs from different genotypes and sexes, as measured by ELISA. **f**, Representative immunofluorescence images of *MAPT*^{P301L} iNeurons treated with BDEVs from different APOE genotypes and sexes. iNeurons were stained for tau misfolded tau protein MC1 (magenta), GFP (green), PKH26-labeled BDEVs (red) and DAPI. Scale bar: 25 μm. **g**, Quantification showed MC1 mean intensity normalized to GFP in *MAPT*^{P301L} iNeurons treated with BDEVs. Female APOE4 BDEVs significantly increased MC1 intensity. One-way ANOVA and Tukey's *post hoc.* All data are presented as mean ± SEM. **h**, Calcium imaging in WT iNeuron of burst correlation indicated neuronal network activity. APOE4/4-BDEV reduced the correlation compared to APOE3/3-BDEV, as determined by the ROC area.

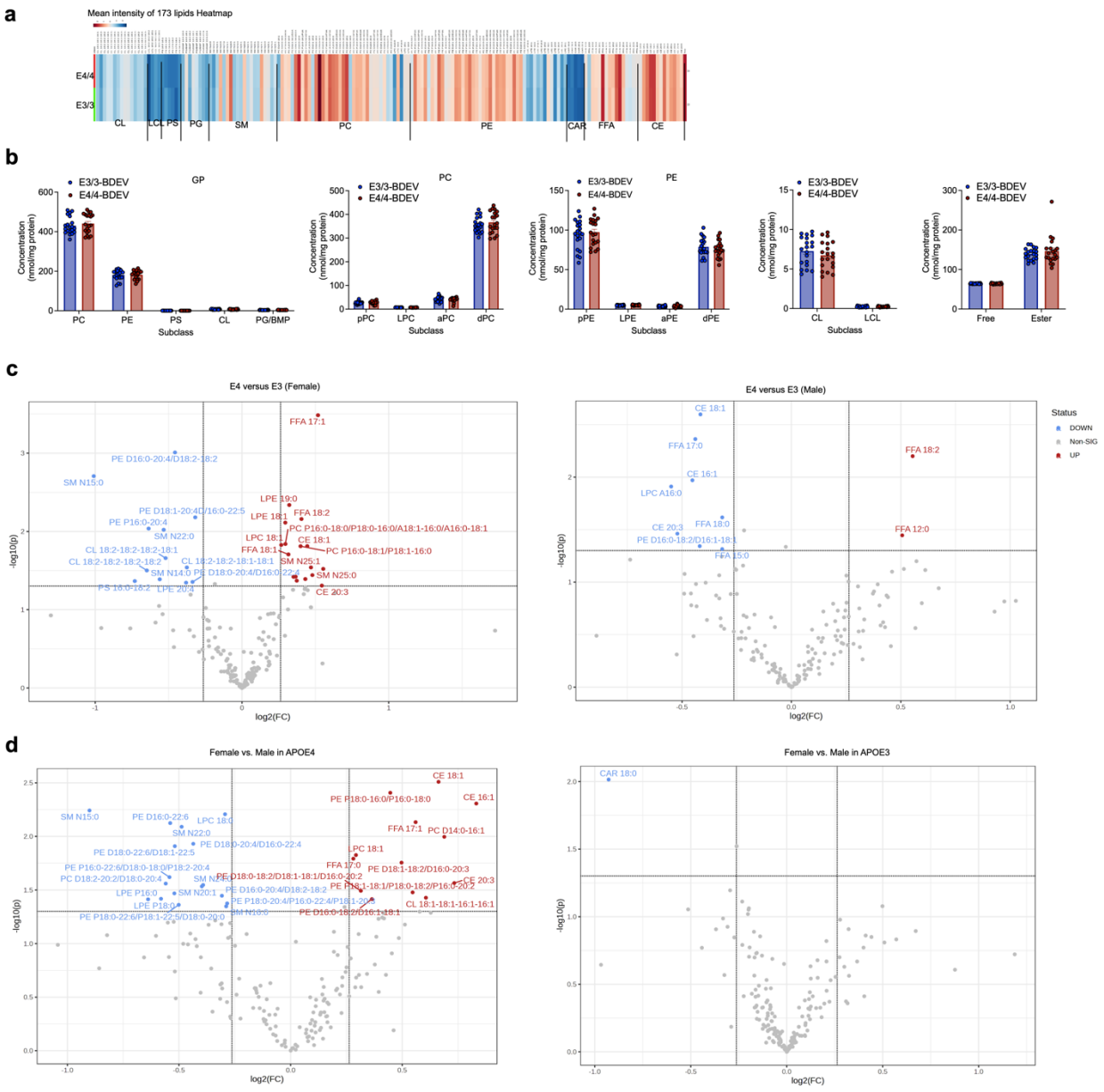

Extended Fig. 6: Lipidomic profiling of APOE3/3 and APOE4/4 BDEVs highlighted distinct lipid signatures and sex-based differences.

a, Heatmap represented the mean intensity of identified 173 lipids across different lipid classes in APOE3/3-BDEVs and APOE4/4-BDEVs. Lipid classes include cardiolipins (CL), lysocardiolipins (LCL), phosphatidylserines (PS), phosphatidylglycerols (PG), sphingomyelins (SM), phosphatidylcholines (PC), phosphatidylethanolamines (PE), acylcarnitines (CAR), free fatty acids (FFA), and cholesterol esters (CE). The heatmap showed lipidomic profiles between two genotype BDEVs, particularly in notable differences among specific lipid classes. **b**, Comparison of glycerophospholipid (GP) subclasses in APOE3/3 and APOE4/4-BDEVs, including phosphatidylcholine (PC), phosphatidylethanolamine (PE), phosphatidylserine (PS),

cardiolipin (CL), and phosphatidylglycerol/bis(monoacylglycero)phosphate (PG/BMP). PC subclasses include plasmalogen PC (pPC), lysophosphatidylcholine (LPC), alkyl-acyl PC (aPC), and diacyl PC (dPC). PE subclasses include plasmalogen PE (pPE), lysophosphatidylethanolamine (LPE), alkyl-acyl PE (aPE), and diacyl PE (dPE). Additionally, cardiolipin (CL), lysocardiolipin (LCL), free and esterified cholesterol lipids, were quantified without difference between APOE3/3 and APOE4/4 BDEVs. **c**, Volcano plot showed the comparisons of lipid differences between APOE4/4 and APOE3/3 BDEVs in females (left panel) and males (right panel). **d,** Volcano plot showed the comparison of lipid molecule differences between female vs. male differences within APOE4/4 (left panel) and APOE3/3 (right panel) genotypes. Upregulated molecules were labeled in red and downregulated molecules labeled in blue with criteria cutoffs of $p < 0.05$ and fold change > 1.2 or < 0.833. All Data are presented as mean ± SEM. The differences were determined multiple t testes.

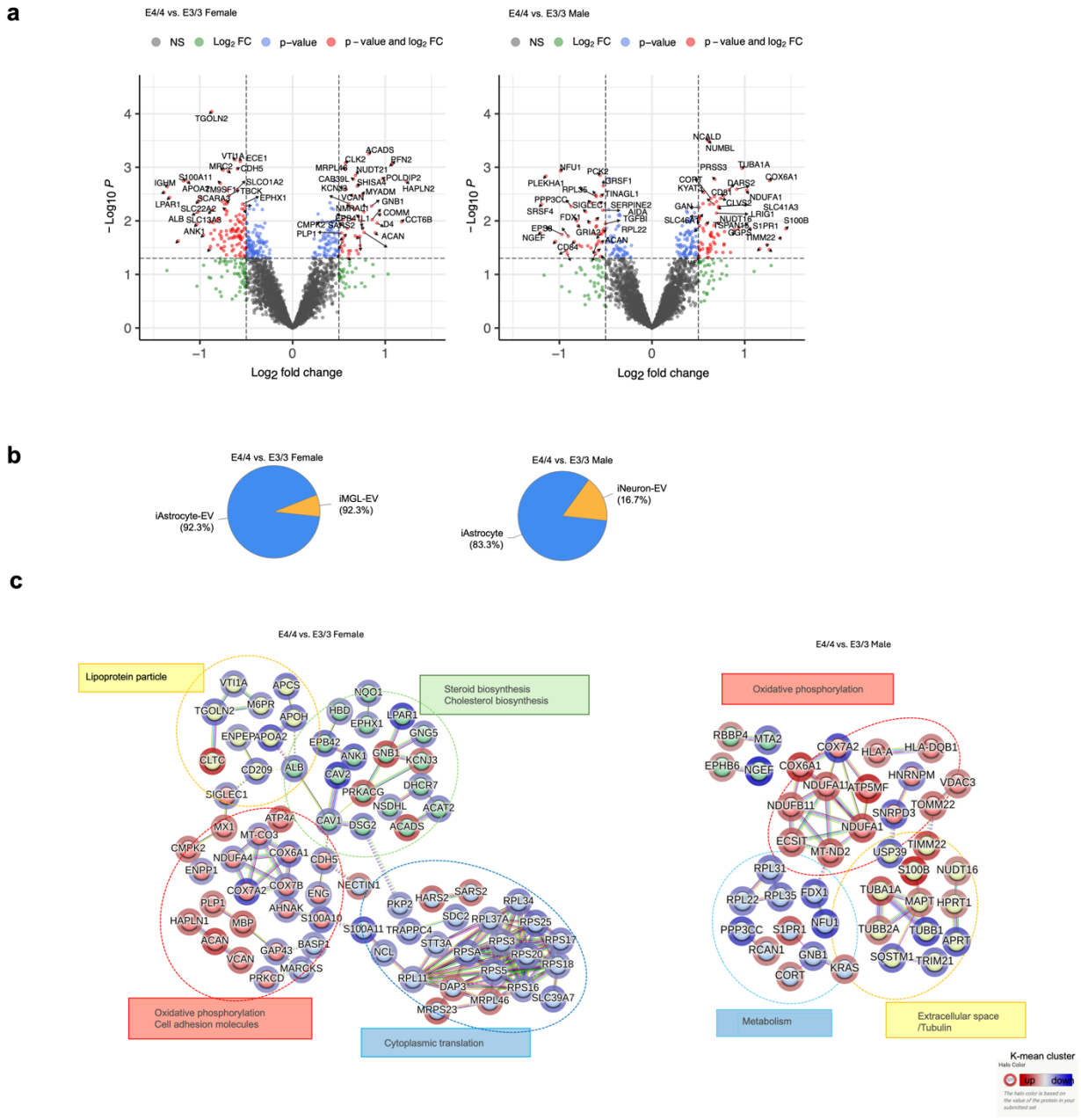

Extended Fig. 7: Differential Expression Analysis of APOE3 and APOE4 BDEVs based on the sex differences.

a, Volcano plots displayed differentially expressed proteins between APOE4 versus APOE3 BDEVs, separated by sex (female left panel and male right panel). Significant proteins are highlighted based on |log2 fold change| > 0.5 and p-value < 0.05 cutoffs. **b,** Differentially expressed proteins (DEPs) between APOE4/4 and APOE3/3 in females (right panel) and males (left panel) were conducted cell-specific enrichment analysis, represented by pie charts indicating enrichment in astrocyte-derived EVs of both, microglia-derived EVs (in females), and neuron-derived EVs (in males). **c,** DEPs between APOE4/4 and APOE3/3 in females and males were

analyzed using the STRING software to construct a protein interaction network. These proteins were mapped to their corresponding Biological Process categories. The top four clusters of protein nodes were determined using k-means clustering, Core proteins, ranked by fold change values, were identified and highlighted within the network. Each cluster is labeled with its respective prominent pathway including lipoprotein particle formation, steroid biosynthesis, oxidative phosphorylation/ cell adhesion molecules and cytoplasmic translation from female groups (left female panel), oxidative phosphorylation, metabolism and extracellular space highlighted in male comparison groups (right male panel). A blue circle represents down-regulation, a red circle represents up-regulation.

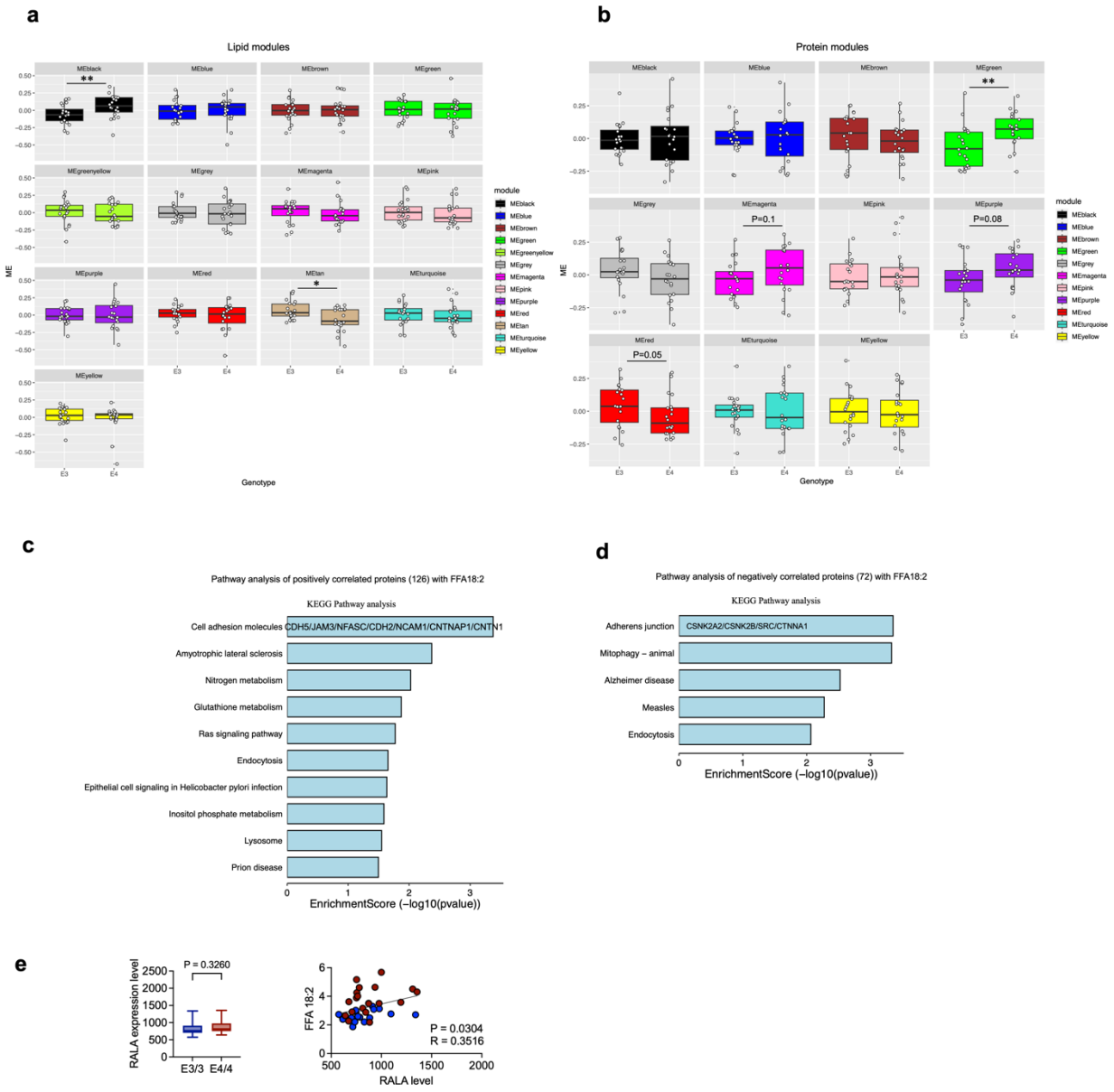

Extended Fig. 8: Lipid and Protein module analysis in APOE3/3 and APOE4/4 BDEVs and the pathway analysis related to FFA18:2.

a, Boxplots displayed the levels of averaged lipid molecules from this lipid module between APOE3/3 and APOE4/4 genotypes, highlighting significant differences in the black and tan lipid modules. Each dot represents an individual case. **b**, Boxplots showed the levels of averaged protein molecules from this module between APOE3/3 and APOE4/4 genotypes, indicating modest differences in the purple, magenta, red and green protein modules. Each dot represents a case, $p < 0.05$ (*), $p < 0.01$ (**) were highlighted. **c**, Pathway analysis of proteins that positively correlated with FFA18:2 revealed top pathways related to cell adhesion molecules, highlighting JAM3, CDH5, CDH2, NFASC, NCAM1, and CNTN1. **d**, Pathway analysis of proteins that

negatively correlated with FFA 18:2 showed enrichment in pathways, including adherent junction with SRC and CTNNA1. **e,** The RALA level from BDEV proteomic data showed no significant difference between the two groups. The correlation between RALA levels and FFA18:2 was positive. Student's t-test and Pearson's correlation were used for analysis.

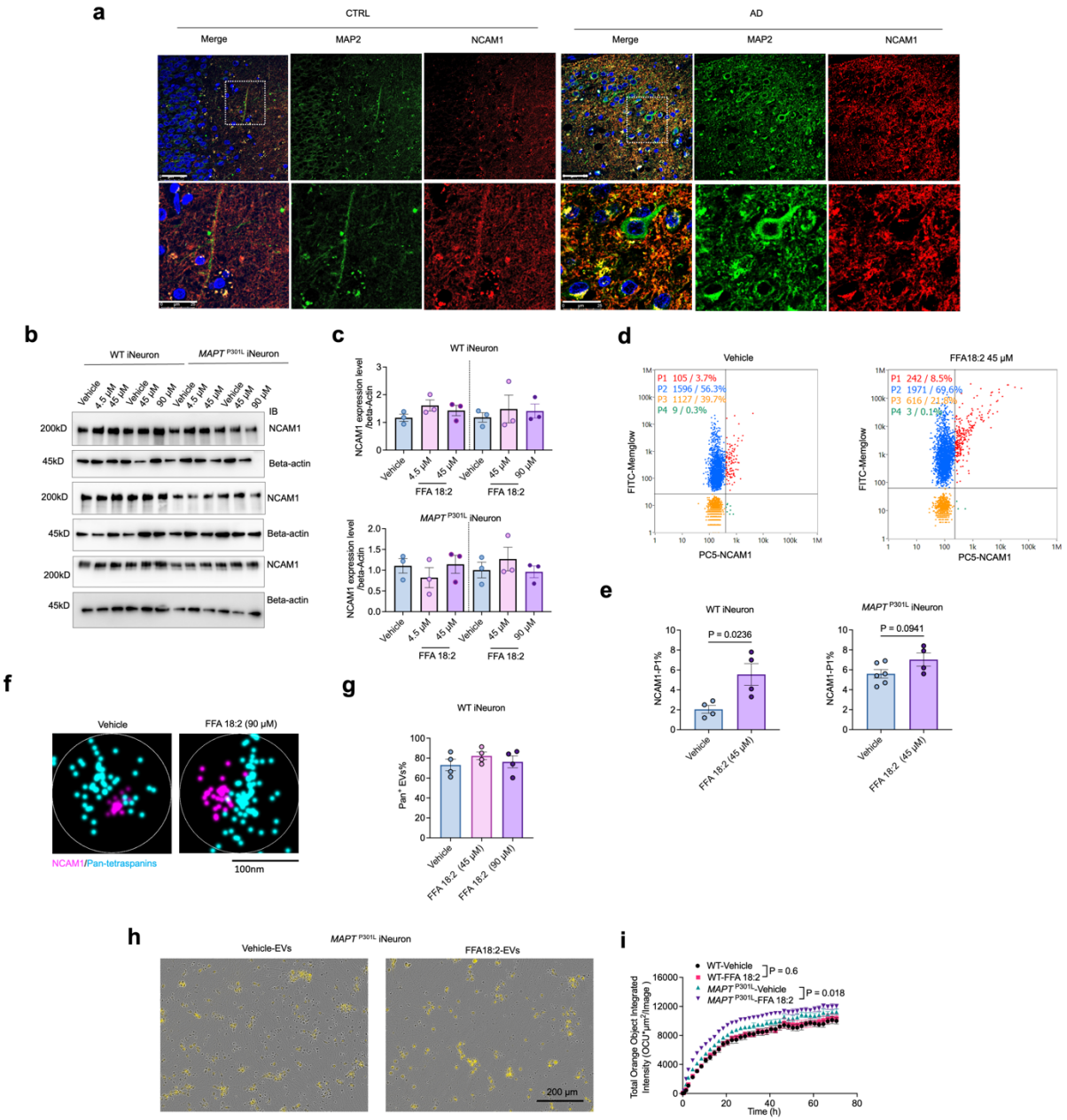

Extended Fig. 9: NCAM1 expression pattern in human brain and its correlation with FFA 18:2 co-contribute to EV mediate pathology.

a, Representative immunofluorescence images of control (CTRL) and Alzheimer's Disease (AD) brain tissue sections, showed MAP2 (green) and NCAM1 (red) expression. Magnified views of selected regions indicated NCAM1 detection within MAP2^{+} neurons. **b**, Western blot analysis of NCAM1 expression in WT and *MAPT*^{P301L} iNeurons treated with varying concentrations of FFA 18:2. Beta-actin was used as a loading control. The results indicate mild, dose-dependent changes in NCAM1 expression in both WT and *MAPT*^{P301L} iNeurons. **c**, Quantification of NCAM1 protein levels in WT and *MAPT*^{P301L} iNeurons from the Western blot analysis was

shown. **d**, Flow cytometry analysis of NCAM1 expression on EVs from WT iNeurons treated with FFA 18:2, detected by Flow Nanoanalyzer. The histograms displayed NCAM1 (conjugated with 647, PC5 channel) and MemGlow-488 (FITC channel) levels in untreated (Vehicle) and FFA 18:2 -treated EVs. **e**, Quantification showed P1 (NCAM1/MemGlow double-positive EVs) in WT and *MAPT*^{P301L} iNeurons, revealing FFA 18:2 treatment increased NCAM1 level on EVs. **f,** Super-resolution microscopy images showed NCAM1 and pan-tetraspanins on EVs isolated from WT iNeurons after FFA 18:2 treatment and controls. The images demonstrated co-localization of NCAM1 with pan-tetraspanins on the EV surface. **g,** Quantification indicated no significant difference in the total number of pan-tetraspanin^{+} EVs following FFA 18:2 treatment. **h,** Representative images of neuronal uptake of EVs derived from either FFA 18:2 or vehicle treated iNeuron in *MAPT*^{P301L} iNeurons. **i**, Time-lapse quantification showed differential uptake of EVs from vehicle versus FFA 18:2-treated iNeurons. The significant difference was determined by ROC area under the curve analysis.

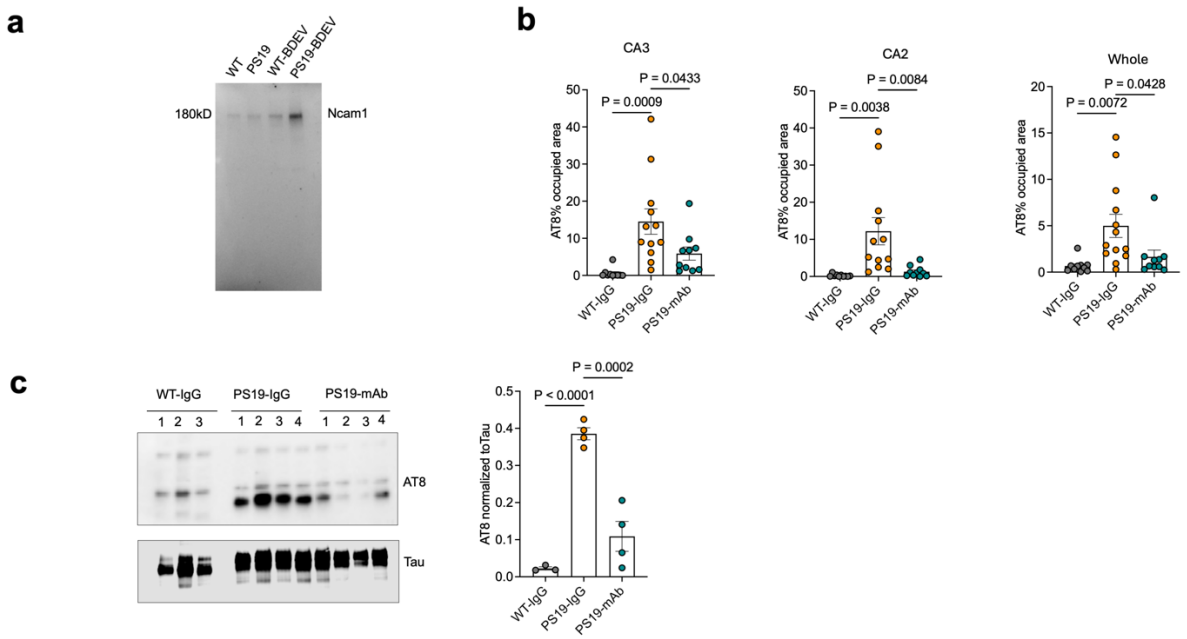

Extended Fig. 10: Anti-NCAM1 immunotherapy attenuated tau propagation in PS19 mice.

a, Western blot analysis and quantification showed increased NCAM1 protein levels of BDEVs from PS19 mouse compared to WT. **b**, Quantification of AT8+ tau pathology in CA3, CA2, and the total cortex and hippocampus (as whole) of PS19 mice, demonstrated a significant reduction following NCAM1 mAb treatment. **c**, Western blot analysis of AT8 and total tau in the RIPA-soluble fraction. Quantification showed the ratio of AT8 normalized to total tau across the three groups. All data are presented as mean ± SEM. Significant difference was determined by One-way ANOVA and Tukey's *post hoc*